

Geophysical Research Letters

RESEARCH LETTER

10.1029/2021GL094585

Key Points:

- Acceleration, Reconnection, Turbulence, and Electrodynamics of the Moon's Interaction with the Sun observes negative surface potentials on the lunar nightside in the magnetotail lobes smaller than expected from tail-plasma charging
- Observed events are concentrated primarily on the lunar dawn hemisphere and are correlated with low ambient plasma densities
- Micrometeoroid impact plasmas are a dominant source of current on the lunar nightside under low-density ambient plasma conditions

Supporting Information:

Supporting Information may be found in the online version of this article.

Correspondence to:

A. R. Poppe,
poppe@ssl.berkeley.edu

Citation:

Poppe, A. R., Xu, S., Liuzzo, L., Halekas, J. S., & Harada, Y. (2021). ARTEMIS observations of lunar nightside surface potentials in the magnetotail lobes: Evidence for micrometeoroid impact charging. *Geophysical Research Letters*, *48*, e2021GL094585. <https://doi.org/10.1029/2021GL094585>

Received 28 MAY 2021

Accepted 17 JUL 2021

ARTEMIS Observations of Lunar Nightside Surface Potentials in the Magnetotail Lobes: Evidence for Micrometeoroid Impact Charging

A. R. Poppe¹ , S. Xu¹ , L. Liuzzo¹ , J. S. Halekas² , and Y. Harada³ 

¹Space Sciences Laboratory, University of California at Berkeley, Berkeley, CA, USA, ²Department of Physics and Astronomy, University of Iowa, Iowa City, IA, USA, ³Department of Geophysics, Kyoto University, Kyoto, Japan

Abstract The Acceleration, Reconnection, Turbulence, and Electrodynamics of the Moon's Interaction with the Sun mission observes anomalously low lunar nightside surface potentials while in the terrestrial magnetotail lobes. Observed potential magnitudes are between 15% and 40% that expected from ambient tail-plasma charging, are highly concentrated on the lunar dawn hemisphere, and are correlated with low ambient plasma densities. These characteristics suggest an additional, highly asymmetric source of cold current to the lunar surface. Given these characteristics, we identify micrometeoroid impact-generated plasmas as the likely source of this additional current. Using laboratory measurements of impact charge yields and models of the micrometeoroid flux to the Moon constrained by in situ measurements, we show that currents due to micrometeoroid impact plasmas have the necessary magnitude and spatial distribution to explain the observed surface potential measurements. Micrometeoroid impact-generated currents may contribute to surface charging at airless bodies with intense micrometeoroid bombardment and/or low ambient plasma densities.

Plain Language Summary Since the Moon lacks a thick atmosphere, both external plasmas and interplanetary micrometeoroids directly interact with the lunar surface. Consequently, the lunar surface builds up a static electric potential that balances all electric currents. NASA's Acceleration, Reconnection, Turbulence, and Electrodynamics of the Moon's Interaction with the Sun (ARTEMIS) mission can remotely determine the electrostatic potential of the lunar surface by observing electrons as they pass by the spacecraft, interact with the lunar surface, and return to the spacecraft with modifications to their flux and energies. We report ARTEMIS observations of lunar surface electrostatic potentials that are not well-described by the theory that only considers contributions from ambient plasma. These observations show that electrostatic potentials on the lunar nightside and dawnside are lower in magnitude than expected, especially when the ambient plasma density is very low. We show that these ARTEMIS observations can be explained by invoking the production of plasma due to interplanetary micrometeoroids impacting the lunar surface. This impact plasma alters the electrostatic charge equilibrium on the lunar surface, leading to lower-than-expected surface potentials. By implication, micrometeoroid impact plasmas may play an important role in the surface charging of airless bodies throughout the solar system, especially when the micrometeoroid flux is particularly high or the ambient plasma flux is particularly low.

1. Introduction

Due to the Moon's lack of a thick, collisional neutral atmosphere, external plasmas can directly interact with the lunar surface and lunar crustal magnetic fields. Among various effects, the flux of external plasmas to the Moon causes the lunar surface to undergo electrostatic charging. Via the use of electron reflectometry (e.g., Anderson et al., 1976; Halekas et al., 2002), surface electrostatic potentials have been well-documented by missions such as Lunar Prospector (LP) (e.g., Halekas et al., 2005, 2007, 2008, 2009a, 2009b; Poppe et al., 2011), Acceleration, Reconnection, Turbulence, and Electrodynamics of the Moon's Interaction with the Sun (ARTEMIS) (e.g., Halekas, Delory, et al., 2011; Halekas et al., 2012; Harada et al., 2013, 2017; Poppe et al., 2012), and Kaguya (Nishino et al., 2017). Comparisons with analytical theory (e.g., Manka, 1973; Sternovsky et al., 2008; Stubbs et al., 2014; Whipple, 1981) and computational models (e.g., Piquette & Horányi, 2017; Poppe & Horányi, 2010) have demonstrated broad agreement in most environments,

implying that our understanding of the equilibrium lunar surface potential as a function of location and ambient environmental parameters is relatively complete. On the lunar dayside, photoemission stimulated by solar ultraviolet radiation is typically the dominant current, thereby yielding positive lunar surface potentials with respect to the ambient plasma. Near the lunar terminators and on the lunar nightside, in contrast, ambient electron collection currents are typically dominant, and lunar surface potentials fall to negative values on the order of the ambient electron temperature. Additional currents from ambient ion collection and secondary electron emission can also affect the current balance and equilibrium surface potential of the Moon.

In addition to ambient plasma, the lunar surface is directly exposed to hypervelocity interplanetary dust impacts originating from both the zodiacal dust cloud and individual meteoroid streams (e.g., Horányi et al., 2015; Janches et al., 2018; Pokorný et al., 2019; Szalay et al., 2018). Hypervelocity dust impacts have long been known to generate impact-vapourization plasmas (e.g., Dietzel et al., 1973; McBride & McDonnell, 1999), which are often used to detect and analyze interplanetary dust fluxes—both by design and fortuitously—throughout the solar system (e.g., Grün, Fechtig, Giese, et al., 1992; Grün, Fechtig, Hanner, et al., 1992; Gurnett et al., 1997; Horányi et al., 2014; Malaspina et al., 2014; Mozer et al., 2020; Srama et al., 2004; Szalay et al., 2020; Ye et al., 2019). Laboratory measurements have quantified the hypervelocity impact-charge yields and impact plasma temperatures as a function of impactor mass and speed (e.g., Collette et al., 2014, 2016), thereby enabling better interpretation of spacecraft measurements. By implication, micrometeoroid impact-generated plasmas, consisting of both ions and electrons, should be generated at the lunar surface. For a negatively biased surface such as the lunar nightside, the impact-generated ions will be immediately recollected while the impact-generated electrons will be repelled from the lunar surface, thereby representing a *net* current source. The nature, magnitude, and variability of such a current at the lunar surface—or to our knowledge, at any airless planetary body—has not previously been considered, quantified, and/or observed.

Here, we report observations by the ARTEMIS mission of “anomalously” small surface potentials on the lunar nightside during times when the Moon was in the low-density terrestrial magnetotail lobes that do not agree with theoretical models of lunar surface charging based on only ambient plasma currents. In Section 2, we describe an example ARTEMIS observation of anomalously small surface potentials, followed by a statistical analysis of dozens of similar events. In Section 3, we present calculations to show that these anomalously small nightside surface potentials can be explained by the consideration of micrometeoroid impact-generated plasma, a heretofore unaddressed source of current at the Moon. Finally, in Section 4, we discuss the implications of our findings for the Moon and airless bodies throughout the solar system.

2. ARTEMIS Observations

The ARTEMIS mission consists of a pair of identical, spin-stabilized spacecraft (P1 and P2) in elliptical orbits around the Moon that continuously measure the ambient plasma and electromagnetic field environment (Angelopoulos, 2011; Sibeck et al., 2011). For this study, we use data from the ARTEMIS Electro-Static Analyzers (McFadden, Carlson, Larson, Bonnell, et al., 2008; McFadden, Carlson, Larson, Ludlam, et al., 2008), the Electric Field Instrument (Bonnell et al., 2008), and the FluxGate Magnetometer (Auster et al., 2008).

2.1. Example Date: February 26, 2021

Figure 1 shows ARTEMIS P1 observations on February 26, 2021 from 20:40 to 21:40 UT including (a) the position of the Moon with respect to the Earth in Geocentric-Solar-Ecliptic coordinates, (b) the trajectories of the P1 and P2 probes with respect to the Moon in Selenocentric-Solar-Ecliptic (SSE) coordinates, (c) the magnetic field vector, (d and e) the downgoing and upgoing electron energy spectra, respectively, (f and g) the downgoing electron density and temperature, respectively, (h) the ratio of the upgoing-to-downgoing electron energy spectra, (i) the solar zenith angle, latitude (“theta”), and longitude (“phi”) of the magnetic field footprint on the lunar surface in SSE coordinates, and (j) the P1 X_{SSE} position. During this period, the Moon and ARTEMIS were in the northern terrestrial magnetotail lobe, as indicated by the $+B_x$ -dominated magnetic field and low densities of $\sim 0.01 \text{ cm}^{-3}$. The ARTEMIS P1 probe crossed the lunar shadow, entering

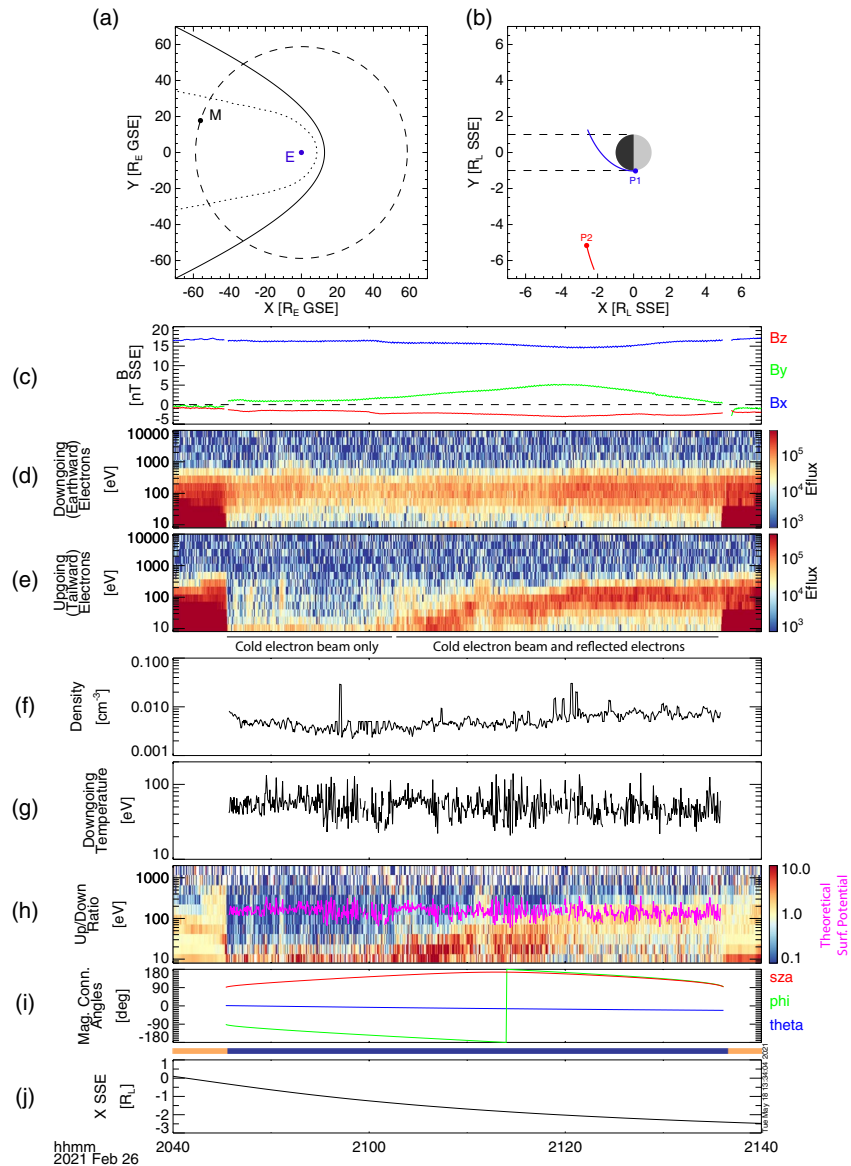


Figure 1. ARTEMIS P1 observations on February 26, 2021 as described in the text. Energy fluxes (“Eflux”) are in units of eV/cm²/s/str/eV. Gaps in the magnetic field near shadow boundaries are due to the removal of data with incomplete despinning.

at $-0.2 R_L$ downstream of the dawn terminator and exiting $-2.4 R_L$ downstream of the dusk terminator. Straight-line magnetic field tracing from the P1 position indicates magnetic connection to the lunar surface throughout the shadow crossing, that is, panel 1(i), although note that the despining algorithm for magnetic fields within eclipse is subject to uncertainties of $\sim 10^\circ$ (Georgescu et al., 2011). The downgoing electron spectra, panel 1(d), show a warm ($T_e \sim 50$ eV) and relatively steady electron population, typical of the magnetotail lobes. Note that periods of high electron flux ($>10^6$ eV/cm²/s/str/eV) at low energies before ($< 20:45$ UT) and after ($>21:35$ UT) the shadow crossing are spacecraft photoelectrons recollected by the ESAs and thus, not geophysical in nature. In contrast, the upgoing electron spectra, panel 1(e), show a series of highly modified distributions. Between $\sim 20:45$ and $21:05$ UT, the upgoing spectra are highly depleted with significant fluxes present for energies less than ~ 20 eV and only minimal presence of reflected electrons near ~ 100 eV (e.g., near 20:51 UT). We note that this period of low-energy upgoing beams occurs when connected to the dawnside hemisphere of the Moon (i.e., $\phi < 0$, panel 1(ii)), a point that we discuss further

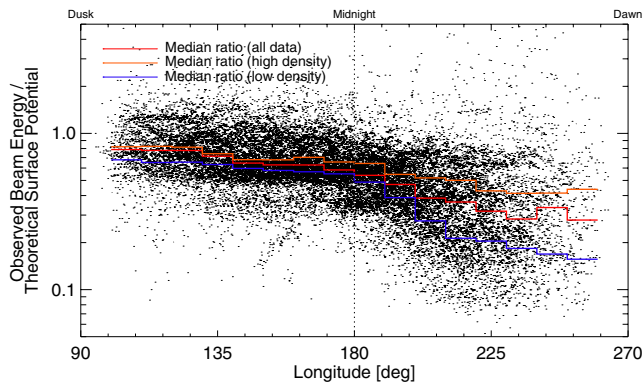


Figure 2. The ratio of observed beam energies to theoretical surface potentials as a function of lunar longitude for all ARTEMIS nightside lobe observations. Colored lines denote the median ratios as a function of longitude for various subsets of the data.

below. Past 21:05, a combination of reflected electrons and a narrow, yet weaker beam of electrons is present, increasing in energy as P1 continues crossing the lunar shadow toward the dusk terminator.

Previous studies of lunar surface charging have shown that the energy of the upgoing electron beam from the lunar surface is highly diagnostic of the potential drop between the Moon and the spacecraft (neglecting the possibility of non-monotonic potentials) (e.g., Halekas et al., 2002, 2005; Poppe et al., 2011, 2012). Thus, we can straightforwardly compare the observed lunar surface potential with theoretical expectations. Adopting the current balance formalism of Manka (1973) (see their Appendix), we can use the observed electron density and temperature, along with previously determined values for the secondary electron emission characteristics of the lunar surface (Halekas et al., 2009a), to compute the theoretically expected lunar surface potential. Specifically, the analytic current-balance calculation includes primary electron and ion collection, and secondary electron emission stimulated by the primary electrons (see full description in the supporting information). For the ion current, we adopt typical values of $T_i = 20$ eV and $v_i = 30$ km/s, as these parameters are not easily

measured or constrained in the low-density magnetotail lobes (e.g., Cao et al., 2020; Liuzzo et al., 2021). Figure 1h shows the theoretical lunar surface potential, overlaid in pink on the upgoing-to-downgoing ratio. The expected lunar surface potential is fairly steady throughout, varying between -115 to -200 V, reasonably in line with previous nightside potentials reported by Halekas et al. (2008). Comparing to the ratio of upgoing-to-downgoing energy spectra, Figure 1e, where the energy of the peak in the ratio indicates the lunar surface potential, we see that between $\sim 21:20 - 21:35$ UT, the theoretical expectation agrees well with the observed upgoing beam. In contrast, between $\sim 20:45 - 21:20$ UT, the observed surface potential is between ≤ -10 V to ≈ -50 V, much smaller in magnitude than expected from theory.

2.2. Statistical Analysis

To further investigate, we searched the entire ~ 10 -year database of ARTEMIS measurements and selected all times during which one of the ARTEMIS probes was magnetically connected to the lunar nightside (using the same straight-line field tracing as above) while in the terrestrial magnetotail lobes. After discarding a limited number of events due to transient phenomena in the tail that complicated further analysis (e.g., flux ropes, plasma sheet boundary layer and/or mantle crossings, etc. [e.g., Hietala et al., 2014; Kiehas et al., 2012; Wang et al., 2014]), we arrived at 55 separate events. These events ranged from 23 to 105 min in length and with the ~ 4 s spin-resolution of the ARTEMIS data set, yielded a total of $N = 28,159$ individual measurements. For each nightside crossing, we retrieved the electron energy spectra, downgoing partial density and temperature, energy of the upgoing electron beam, and longitude of the magnetic footpoint on the lunar surface. From these data, we used the downgoing density and temperature to calculate the theoretical lunar surface potential using the same analytical theory described above (Manka, 1973) for the February 26, 2021 event.

Figure 2 shows the statistical distribution of the ratio of the observed upgoing electron beam energy to the theoretically calculated surface potential as a function of the SSE longitude of the magnetic footpoint on the lunar surface for all 55 identified events. Over-plotted as colored lines are the median ratios versus longitude within 10° bins for: all data points (red), those data points with downgoing densities greater than the median density (orange), and those data points with downgoing densities less than the median density (blue). Between the dusk terminator (90°) and midnight (180°), the distribution and median values lie only slightly below unity (median ratio ≈ 0.8), indicating that the surface charging theory describes the data generally well. The slight mismatch between the model and data here is likely due to a bias in either the secondary electron emission yield, δ_M , or the properties of the magnetotail lobe ion population, both of which are difficult to precisely constrain (e.g., Cao et al., 2020; Halekas et al., 2009a; Liuzzo et al., 2021). In contrast, between midnight and the dawn terminator (270°), the ratio of the observed-to-theoretical surface potentials falls well below unity, indicating that the lunar surface potential is smaller in magnitude (i.e., less

negative) than theory predicts. Furthermore, this effect is more pronounced for cases with lower ambient plasma density, that is, the low-density median values (blue) are smaller than the high-density median values (orange). We interpret this data-theory disagreement as evidence of an additional, net-positive current to the lunar nightside that (a) is concentrated nearly exclusively on the lunar dawn hemisphere and (b) is relatively weak in magnitude, such that its effects are generally more important when the ambient density (and thus ambient electron current) is lower.

3. Micrometeoroid Impact Charging

Given the particular characteristics of the observed disagreement between the ARTEMIS observations and the current-balance theory, we propose and quantitatively demonstrate that currents arising from micrometeoroid impact-generated plasma have the correct magnitude and spatial characteristics to explain the deviation of the nightside lunar surface potential from theoretical expectations that only account for currents from ambient plasmas. The magnitude of the micrometeoroid impact-generated current at the Moon can be calculated with knowledge of the impacting micrometeoroid mass and velocity distributions, combined with an appropriate scaling law for the impact-charge production as a function of mass and velocity, $Q_{imp}(m, v) = Cmv^\gamma$, where C and γ are empirically derived coefficients. While significant previous work has explored this relation (e.g., Dietzel et al., 1973; Göller & Grün, 1989; Grün, 1984; Grün et al., 2007; McBride & McDonnell, 1999; Srama et al., 2004), we adopt recent results from Collette et al. (2014), which reported impact-charge yield measurements for iron impactors onto five separate materials: silver, beryllium copper, multilayer thermal insulation, germanium-coated Kapton, and solar cell material. Despite differences in the target materials, Collette et al. (2014) found only moderate variation in the $Q(m, v)$ relation for impact-charge production. Such insensitivity to the impact material suggests that the parameters determined in Collette et al. (2014) should reasonably apply for lunar regolith, and we adopt this assumption for the following calculations. We also note that the use of iron impactors is not perfectly appropriate for interplanetary micrometeoroid impacts; however, no other impactor types were used by Collette et al. (2014). We take the median values of the scaling parameters, giving an impact charge relation of,

$$Q(m, v) = 0.005mv^{4.2}, \quad (1)$$

where m is the impactor mass in kg, v is the impactor speed in km/s, and Q is the impact charge in C. The strong scaling of the impact charge with velocity ($Q \propto v^{4.2}$; Collette et al., 2014) implies that the fastest impacting meteoroids will contribute the most to the overall impact-charge production.

The best-fit micrometeoroid impact velocity distribution onto the lunar surface is shown in Figure 3a, as derived by Pokorný et al. (2019) (see their Figure 5). The impact velocity distribution is comprised of several sub-populations, with local peaks near ~ 8 km/s and ~ 55 km/s, and an additional shoulder near 25 km/s, representing various contributions from main-belt asteroids, Jupiter-family comets, Halley-type comets, and Oort Cloud comets. As discussed in Pokorný et al. (2019), the fastest impactors originate from a combination of Oort Cloud and Halley-type impactors, while slower impactors generally originate from Jupiter-family and asteroidal dust grains. Figure 3b shows the relative impact charge production as a function of impact velocity, calculated by scaling the micrometeoroid velocity distribution shown in panel 3(a) by $v^{4.2}$. Given the strong velocity scaling, meteoroids with velocities less than 45 km/s contribute only $\approx 20\%$ to the total impact charge while velocities greater than 45 km/s contribute $\approx 80\%$ of the impact charge. To calculate the net micrometeoroid impact current density, J_d , we adopt the *relative* mass distribution of Grün et al. (1985), normalize the mass distribution such that the total mass flux to the Moon matches the globally averaged value of $\sim 1,450$ kg/day as determined by Pokorný et al. (2019), and convolve the mass distribution with the impact charge function, $Q(m, v)$. The globally averaged micrometeoroid-impact current is, $J_d \approx 10^{-10}$ A/m², although likely with large error bars due to uncertainties in (a) the net mass flux to the Moon, (b) the micrometeoroid impact velocity distribution at the Moon, and (c) the impact-charge scaling law. Regarding this last point, we re-calculated the net micrometeoroid impact current for all five values of $[C, \gamma]$ reported by Collette et al. (2014) and found net variations on the order of ≈ 5 , indicating moderate uncertainty in this relation. Conservatively, we estimate an order-of-magnitude uncertainty for the net current, J_d , due to the multiple compounding sources of error.

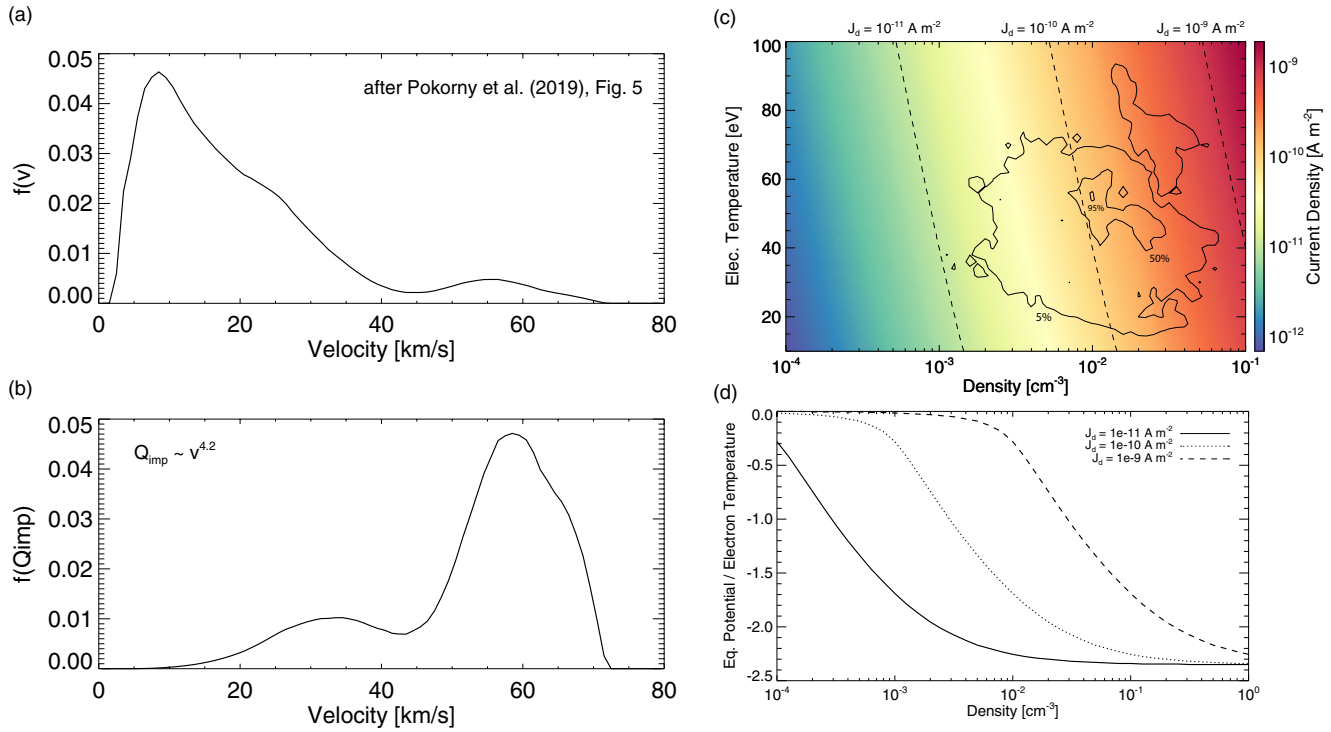


Figure 3. (a) The relative micrometeoroid-impact velocity distribution at the Moon, from Pokorný et al. (2019). (b) The relative micrometeoroid-impact charge production distribution at the Moon as a function of velocity. (c) The primary electron current density to the lunar surface at the equilibrium potential without the presence of micrometeoroid impact-generated current. Overplotted as irregular contour lines are the 5%, 50% (median), and 95% contours of the ARTEMIS observations in the magnetotail lobes. The dashed curves denote micrometeoroid impact current densities of $J_d = 10^{-11}$ A m⁻², 10^{-10} A m⁻², and 10^{-9} A m⁻². (d) The equilibrium potential of the lunar surface normalized by the ambient electron temperature as a function of the ambient plasma density, including micrometeoroid impact-generated currents at three magnitudes.

A micrometeoroid-impact charging current of $J_d \approx 10^{-10}$ A/m² is sufficient to significantly alter the lunar nightside potential in the magnetotail lobes. As a first-order comparison, Figure 3c shows the primary magnetotail electron current to the lunar surface as a function of the ambient density and electron temperature at the equilibrium potential *without* the inclusion of any micrometeoroid impact-generated currents (see Equation S5). The irregularly shaped contours overplotted on Figure 3c show the 5%, median (50%), and 95% occurrence-rate boundaries for the distribution of densities and temperatures from the selected ARTEMIS magnetotail lobe observations (i.e., corresponding to those data shown in Figure 2). Over the range of densities and temperatures observed by ARTEMIS, the primary electron current varies between $\sim 10^{-11}$ A m⁻² to 10^{-9} A m⁻². In comparison, the dashed curves show current densities of 10^{-11} , 10^{-10} , and 10^{-9} A m⁻², corresponding to the median micrometeoroid impact-generated current densities and an order-of-magnitude both above and below. The 10^{-10} A m⁻² current density falls very close to the peak of the observed distribution of ARTEMIS events, while the range of errors (spanning 10^{-11} A m⁻² to 10^{-9} A m⁻²) brackets the entire range of observed ARTEMIS events to the 5% level. Thus, to first order, the inclusion of a micrometeoroid-impact current should play a significant role in altering the current balance of the lunar nightside.

To this end, we addressed the effects of the micrometeoroid-impact current more quantitatively by using the same Manka (1973) current balance formalism as before, but now with four current sources: ambient primary electrons, ambient primary ions, surface secondary electrons, and the micrometeoroid-impact current (see Equation S6). Figure 3d shows the equilibrium nightside lunar surface potential normalized to the ambient electron temperature as a function of the ambient plasma density for three values of the micrometeoroid-impact current, $J_d = [10^{-11}, 10^{-10}, 10^{-9}]$ A m⁻², which bracket the median value with one order-of-magnitude uncertainty. For this calculation, we used a canonical value of $T_e = 50$ eV for the ambient electron temperature, approximately corresponding to the most likely observed temperature (i.e., Figure 3c). At relatively large ambient plasma densities ($n > 0.1$ cm⁻³), the $J_d = 10^{-11}$ and 10^{-10} A m⁻²

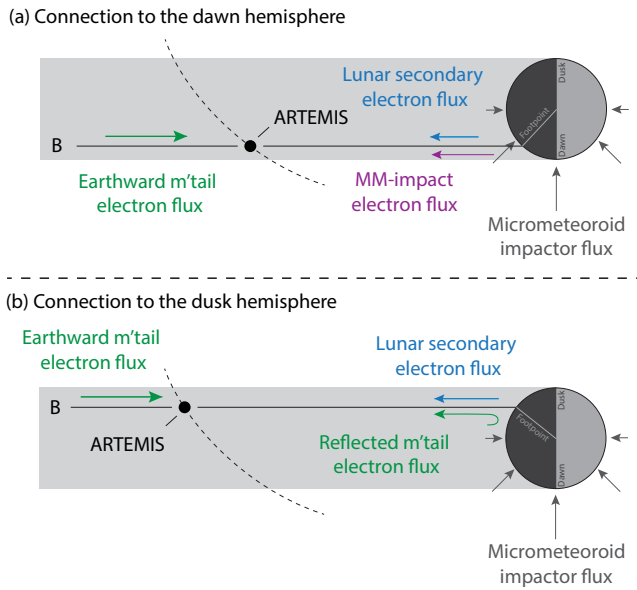


Figure 4. (a and b) Cartoons describing the relevant geometry and electron fluxes for periods of connection to dawn and dusk hemispheres, respectively.

conditions produce only minor changes (i.e., < 10%) to the equilibrium potential, while the $J_d = 10^{-9} \text{ A m}^{-2}$ case reduces the surface potential by $\approx 25\%$. In contrast, at lower densities more typical of the magnetotail lobes, $n \approx 10^{-2} \text{ cm}^{-3}$, the micrometeoroid-impact current has a strong effect on the lunar surface potential. For the $J_d = 10^{-9}$ case, surface potentials are reduced to <10% their “nominal” value, while for the $J_d = 10^{-10}$ case, potentials are reduced by $\approx 33\%$. At the lowest ambient densities observed by ARTEMIS, $n \approx 10^{-3} \text{ cm}^{-3}$, both the $J_d = 10^{-9}$ and $J_d = 10^{-10}$ cases have reduced the surface potential by >90%, while even the lowest bound for the micrometeoroid current, $J_d = 10^{-11}$, has reduced the surface potential by $\approx 33\%$. Notably, this range of reduced potentials due to the presence of the micrometeoroid-impact current falls within the range of reduced potentials observed by ARTEMIS as shown in Figure 2. Thus, the micrometeoroid-impact current is a plausible and likely mechanism operating continuously at the Moon, yet typically only observable during low plasma density conditions on the lunar night and dawnside via its effect on electrostatic surface potentials.

Finally, the angular distribution of the impacting micrometeoroid flux at the Moon is consistent with the observed longitudinal distribution of low-magnitude surface potentials observed by ARTEMIS as shown in Figure 2. In situ observations by the LADEE/LDEX instrument (Horányi et al., 2014, 2015; Szalay & Horányi, 2015), combined with a dynamical model of the interplanetary dust distribution (Janches et al., 2018;

Pokorný et al., 2019), have shown that the micrometeoroid flux to the Moon is highly concentrated on the dawn hemisphere of the Moon, albeit with significant sub-structure (Horányi et al., 2015; Szalay & Horányi, 2015), similar to that observed at Earth (e.g., Campbell-Brown, 2008; Janches et al., 2006; Pokorný et al., 2017). As diagrammed in Figure 4, the lunar nightside charging environment is driven by several sources of current including earthward magnetotail electron flux (minus any reflected magnetotail electron flux due to near-surface potentials or crustal magnetic fields), lunar secondary electron flux stimulated by energetic primary electrons that impact the surface, and the micrometeoroid impact-generated electron flux. Magnetotail ion fluxes are also present, but are a minor contributor. As noted above, the micrometeoroid flux and its associated impact-generated plasma are concentrated on the dawn hemisphere of the Moon. For a negatively biased surface, the impact-plasma ions are recollected while the impact-plasma electrons are repelled, thus providing a net current to the lunar surface concentrated on the dawn hemisphere, panel 4(a). In contrast, on the dusk hemisphere, panel 4(b), the micrometeoroid impact-generated plasma is highly diminished—if not entirely negligible—due to the relative decrease in micrometeoroid flux to the dusk hemisphere and surface charging is primarily controlled by ambient plasma currents only. Thus, the spatial distribution of the micrometeoroid-impact current agrees well with the deviations from theoretical predictions seen in the ARTEMIS data as a function of longitude, Figure 2.

4. Discussion and Conclusion

We have presented ARTEMIS observations, both individually and in aggregate, of lunar nightside electrostatic potentials in the terrestrial magnetotail lobes that are lower in magnitude than expected from current-balance theory with plasma currents only. The statistical distribution of these events reveals that they are highly correlated with magnetic connection to the lunar dawnside hemisphere and with decreasing ambient plasma densities. Currents arising from micrometeoroid-impact plasma satisfy both the spatial distribution of the observed deviations due to the strong, dawn-centered asymmetry of the impact micrometeoroid flux (Horányi et al., 2015; Pokorný et al., 2019; Szalay & Horányi, 2015), as well as the magnitude of the current required to produce the observed deviations in the surface potential. By logical extension, one may also consider that meteoroid streams, which have highly asymmetric bombardment patterns and typical impact velocities much higher than the background zodiacal cloud (e.g., Benna et al., 2019; Oberst & Nakamura, 1987; Szalay & Horányi, 2016; Szalay et al., 2018), could potentially alter the lunar nightside

surface potentials at their sub-radiant points, if such streams coincided with lunar passages through the low-density magnetotail lobes. In the solar wind, deviations from expected surface potentials could also be present on the lunar nightside, as the lunar wake provides a local, low-density plasma environment; however, we note that remote electron reflectometry measurements of the lunar surface potential—and any alteration thereof by micrometeoroid-impact currents—is likely to be obfuscated by the presence of electrostatic potentials driven by the solar wind refilling processes in the lunar wake (e.g., Halekas, Angelopoulos, et al., 2011; Xu et al., 2019). Finally, the micrometeoroid impact-generated current also has implications for the electrostatic environment within shadowed craters at the Moon. Previous work has suggested that the leeward sides of lunar craters may be exposed to an electron-rich environment such that excessively large negative potentials could build up at the surface (e.g., Farrell et al., 2007, 2010; Farrell, Stubbs, Delory, et al., 2008; Farrell, Stubbs, Halekas, et al., 2008; Zimmerman et al., 2011); however, the micrometeoroid impact-generated current could provide a “current of last resort” by stimulating the emission and escape of electrons from the surface, thereby lowering any excessively large electrostatic potentials. Further exploration of the interaction of ambient plasma currents, micrometeoroid-impact currents, and lunar crustal magnetic fields (which may also impact the incident current) is clearly warranted, in particular via particle-in-cell models capable of kinetically tracking all relevant species.

The discovery and characterization of a micrometeoroid impact-generated current at the Moon has natural implications for other airless bodies throughout the solar system. In particular, objects subjected to a combination of high-flux and/or high-velocity micrometeoroid bombardment and relatively low ambient plasma currents may have surface potentials significantly altered. At Mercury, for example, micrometeoroid impact velocities are significantly higher than at the Moon, reaching over 100 km/s (Pokorný et al., 2018), while Mercury’s intrinsic magnetosphere may yield relatively low-density regions within closed magnetospheric fields (e.g., Raines et al., 2013). The strong scaling of impact-charge production on the micrometeoroid impact velocities implies that equilibrium surface potentials within Mercury’s closed-field line regions are likely to be strongly altered. The Martian, Jovian, and Saturnian satellites may also be subject to significant micrometeoroid impact-generated currents. In the cases of Phobos and Deimos at Mars, passage through the low-density martian magnetotail may provide a low plasma-current environment in which micrometeoroid impact currents could dominate (e.g., Nénon et al., 2019). In contrast, the Jovian and Saturnian satellites are not typically subjected to such low ambient densities (with the exceptions of Callisto and regions within Ganymede’s closed field lines) (e.g., Kivelson et al., 2004; Roussos et al., 2010); however, the gravitational focusing and acceleration of interplanetary micrometeoroids by their parent planets (e.g., Poppe, 2016; Spahn et al., 2006) may increase the micrometeoroid-impact current to levels high enough to compete with ambient plasma currents.

Data Availability Statement

All ARTEMIS data are publicly available at http://artemis.ssl.berkeley.edu/data_files.shtml.

References

- Anderson, K. A., Lin, R. P., McCoy, J. E., & McGuire, R. E. (1976). Measurements of lunar and planetary magnetic fields by reflection of low energy electrons. *Space Science Instrumentation*, 1, 439–470.
- Angelopoulos, V. (2011). The ARTEMIS mission. *Space Science Reviews*, 165, 3–25. <https://doi.org/10.1007/s11214-010-9687-2>
- Auster, H. U., Glassmeier, K. H., Magnes, W., Aydogar, O., Baumjohann, W., Constantinescu, D., et al. (2008). The THEMIS fluxgate magnetometer. *Space Science Reviews*. <https://doi.org/10.1007/s11214-008-9365-9>
- Benna, M., Hurlay, D. M., Stubbs, T. J., Mahaffy, P. R., & Elphic, R. C. (2019). Lunar soil hydration constrained by exospheric water liberated by meteoroid impacts. *Nature Geoscience*, 12, 333–338. <https://doi.org/10.1038/s41561-019-0345-3>
- Bonnell, J. W., Mozer, F. S., Delory, G. T., Hull, A. J., Ergun, R. E., Cully, C. M., et al. (2008). The electric field instrument (EFI) for THEMIS. *Space Science Reviews*, 141, 303–341. <https://doi.org/10.1007/s11214-008-9469-2>
- Campbell-Brown, M. D. (2008). High resolution radiant distribution and orbits of sporadic radar meteoroids. *Icarus*, 196, 144–163. <https://doi.org/10.1016/j.icarus.2008.02.022>
- Cao, X., Halekas, J. S., Chu, F., Kistler, M., Poppe, A. R., & Glassmeier, K.-H. (2020). Plasma convection in the terrestrial magnetotail lobes measured near the Moon’s orbit. *Geophysical Research Letters*, 47, e2020GL090217. <https://doi.org/10.1029/2020GL090217>
- Collette, A., Grün, E., Malaspina, D., & Sternovsky, Z. (2014). Micrometeoroid impact charge yield for common spacecraft materials. *Journal of Geophysical Research: Space Physics*, 119, 6019–6026. <https://doi.org/10.1002/2014JA020042>
- Collette, A., Malaspina, D. M., & Sternovsky, Z. (2016). Characteristic temperatures of hypervelocity dust impact plasmas. *Journal of Geophysical Research: Space Physics*, 121, 8182–8187. <https://doi.org/10.1002/2015ja022220>

Acknowledgments

The authors acknowledge NASA’s Lunar Data Analysis Program, Grants #80NSSC18K1565 and #80NSSC20K0311. A. R. Poppe and J. S. Halekas also acknowledge NASA SSERVI’s LEADER team, Grants #80NSSC20M0060 and #80NSSC20M0022. The authors acknowledge NASA contract NAS5-02099 and V. Angelopoulos for the use of ARTEMIS data; specifically, J. W. Bonnell and F. S. Mozer for the use of EFI data, C. W. Carlson and J. P. McFadden for the use of ESA data, and K. H. Glassmeier, U. Auster, and W. Baumjohann for the use of FGM data provided under the lead of the Technical University of Braunschweig and with financial support through the German Ministry for Economy and Technology and the German Center for Aviation and Space (DLR) under contract 50-OC-0302.

- Dietzel, H., Eichhorn, G., Fechtig, H., Grün, E., Hoffman, H.-J., & Kissel, J. (1973). The HEOS2 and HELIOS micrometeoroid experiments. *Journal of Physics E: Scientific Instruments*, 6(3), 209–217. <https://doi.org/10.1088/0022-3735/6/3/008>
- Farrell, W. M., Stubbs, T. J., Delory, G. T., Vondrak, R. R., Collier, M. R., Halekas, J. S., & Lin, R. P. (2008b). Concerning the dissipation of electrically charged objects in the shadowed lunar polar regions. *Geophysical Research Letters*, 35, L19104. <https://doi.org/10.1029/2008gl034785>
- Farrell, W. M., Stubbs, T. J., Halekas, J. S., Delory, G. T., Collier, M. R., Vondrak, R. R., & Lin, R. P. (2008a). Loss of solar wind plasma neutrality and affect on surface potentials near the lunar terminator and shadowed polar regions. *Geophysical Research Letters*, 35, L05105. <https://doi.org/10.1029/2007gl032653>
- Farrell, W. M., Stubbs, T. J., Halekas, J. S., Killen, R. M., Delory, G. T., Collier, M. R., & Vondrak, R. R. (2010). Anticipated electrical environment within permanently shadowed lunar craters. *Journal of Geophysical Research*, 115, E03004. <https://doi.org/10.1029/2009je003464>
- Farrell, W. M., Stubbs, T. J., Vondrak, R. R., Delory, G. T., & Halekas, J. S. (2007). Complex electric fields near the lunar terminator: The near-surface wake and accelerated dust. *Geophysical Research Letters*, 34, L14201. <https://doi.org/10.1029/2007gl029312>
- Georgescu, E., Plaschke, F., Auster, U., Fornacon, K.-H., & Frey, H. U. (2011). Modelling of spacecraft spin period during eclipse. *Annales Geophysicae*, 29, 875–882. <https://doi.org/10.5194/angeo-29-875-2011>
- Göller, J. R., & Grün, E. (1989). Calibration of the Galileo/Ulysses dust detectors with different projectile materials and at varying impact angles. *Planetary and Space Science*, 37(10), 1197–1206. [https://doi.org/10.1016/0032-0633\(89\)90014-7](https://doi.org/10.1016/0032-0633(89)90014-7)
- Grün, E. (1984). Impact ionization from gold, aluminum, and PCB-Z. *ESA Special Publications*, 224, 39–41.
- Grün, E., Fechtig, H., Giese, R. H., Kissel, J., Linkert, D., Maas, D., et al. (1992). The Ulysses dust experiment. *Astronomy and Astrophysics Supplement Series*, 92, 411–423.
- Grün, E., Fechtig, H., Hanner, M. S., Kissel, J., Lindblad, B.-A., Linkert, D., et al. (1992). The Galileo dust detector. *Space Science Reviews*, 60, 317–340. https://doi.org/10.1007/978-94-011-2512-3_13
- Grün, E., Pawlinka, S., & Srama, R. (2007). *Dust accelerator tests with Cassini RPWS samples* (Technical Report). MPI-K.
- Grün, E., Zook, H. A., Fechtig, H., & Giese, R. H. (1985). Collisional balance of the meteoric complex. *Icarus*, 62, 244–272. [https://doi.org/10.1016/0019-1035\(85\)90121-6](https://doi.org/10.1016/0019-1035(85)90121-6)
- Gurnett, D. A., Ansher, J. A., Kurth, W. S., & Granroth, L. J. (1997). Micron-sized dust particles detected in the outer solar system by the Voyager 1 and 2 plasma wave instruments. *Geophysical Research Letters*, 24(24), 3125–3128. <https://doi.org/10.1029/97gl03228>
- Halekas, J. S., Angelopoulos, V., Sibeck, D. G., Khurana, K. K., Russell, C. T., Delory, G. T., et al. (2011). First results from ARTEMIS, a new two-spacecraft Lunar Mission: Counter-streaming plasma populations in the Lunar Wake. *Space Science Reviews*, 165, 93–107. https://doi.org/10.1007/978-1-4614-9554-3_5
- Halekas, J. S., Delory, G. T., Brain, D. A., Lin, R. P., Fillingim, M. O., Lee, C. O., et al. (2007). Extreme lunar surface charging during solar energetic particle events. *Geophysical Research Letters*, 34, L02111. <https://doi.org/10.1029/2006gl028517>
- Halekas, J. S., Delory, G. T., Farrell, W. M., Angelopoulos, V., McFadden, J. P., Bonnell, J. W., et al. (2011). First remote measurements of lunar surface charging from ARTEMIS: Evidence for nonmonotonic sheath potentials above the dayside surface. *Journal of Geophysical Research*, 116, A07103. <https://doi.org/10.1029/2011ja016542>
- Halekas, J. S., Delory, G. T., Lin, R. P., Stubbs, T. J., & Farrell, W. M. (2008). Lunar Prospector observations of the electrostatic potential of the lunar surface and its response to incident currents. *Journal of Geophysical Research*, 113, A09102. <https://doi.org/10.1029/2008ja013194>
- Halekas, J. S., Delory, G. T., Lin, R. P., Stubbs, T. J., & Farrell, W. M. (2009a). Lunar prospector measurements of secondary electron emission from lunar regolith. *Planetary and Space Science*, 57, 78–82. <https://doi.org/10.1016/j.pss.2008.11.009>
- Halekas, J. S., Delory, G. T., Lin, R. P., Stubbs, T. J., & Farrell, W. M. (2009b). Lunar surface charging during solar energetic particle events: Measurement and prediction. *Journal of Geophysical Research*, 114, A05110. <https://doi.org/10.1029/2009ja014113>
- Halekas, J. S., Lin, R. P., & Mitchell, D. L. (2005). Large negative lunar surface potentials in sunlight and shadow. *Geophysical Research Letters*, 32, L09102. <https://doi.org/10.1029/2005gl022627>
- Halekas, J. S., Mitchell, D. L., Lin, R. P., Hood, L. L., Acuña, M. H., & Binder, A. B. (2002). Evidence for negative charging of the lunar surface in shadow. *Geophysical Research Letters*, 29(10), 1435. <https://doi.org/10.1029/2001gl014428>
- Halekas, J. S., Poppe, A. R., Farrell, W. M., Delory, G. T., Angelopoulos, V., McFadden, J. P., et al. (2012). Lunar precursor effects in the solar wind and terrestrial magnetosphere. *Journal of Geophysical Research*, 117, A05101. <https://doi.org/10.1029/2011ja017289>
- Harada, Y., Machida, S., Halekas, J. S., Poppe, A. R., & McFadden, J. P. (2013). ARTEMIS observations of lunar dayside plasma in the terrestrial magnetotail lobe. *Journal of Geophysical Research*, 118, 1–8. <https://doi.org/10.1002/jgra.50296>
- Harada, Y., Poppe, A. R., Halekas, J. S., Chamberlin, P. C., & McFadden, J. P. (2017). Photoemission and electrostatic potentials on the dayside lunar surface in the terrestrial magnetotail lobes. *Geophysical Research Letters*, 44, 5276–5282. <https://doi.org/10.1002/2017GL073419>
- Hietala, H., Eastwood, J. P., & Isavnin, A. (2014). Sequentially released tilted flux ropes in the Earth's magnetotail. *Plasma Physics and Controlled Fusion*, 56, 064011. <https://doi.org/10.1088/0741-3335/56/6/064011>
- Horányi, M., Sternovsky, Z., Lankton, M., Dumont, C., Gagnard, S., Gathright, D., et al. (2014). The Lunar Dust Experiment (LDEX) onboard the Lunar Atmosphere and Dust Environment Explorer (LADEE) mission. *Space Science Reviews*, 185, 93–113. <https://doi.org/10.1007/s11214-014-0118-7>
- Horányi, M., Szalay, J. R., Kempf, S., Schmidt, J., Grün, E., Srama, R., & Sternovsky, Z. (2015). A permanent, asymmetric dust cloud around the Moon. *Nature*, 522, 324–326. <https://doi.org/10.1038/nature14479>
- Janches, D., Heinselman, C. J., Chau, J. L., Chandran, A., & Woodman, R. (2006). Modeling the global micrometeor input function in the upper atmosphere observed by high power and large aperture radars. *Journal of Geophysical Research*, 111, A07317. <https://doi.org/10.1029/2006ja011628>
- Janches, D., Pokorný, P., Sarantos, M., Szalay, J. R., Horányi, M., & Nesvorný, D. (2018). Constraining the ratio of micrometeoroids from short- and long-period comets at 1 AU from LADEE observations of the lunar dust cloud. *Geophysical Research Letters*, 45, 1713–1722. <https://doi.org/10.1002/2017GL076065>
- Kiehas, S. A., Angelopoulos, V., Runov, A., Moldwin, M. B., & Möstl, C. (2012). On the formation of tilted flux ropes in the Earth's magnetotail observed with ARTEMIS. *Journal of Geophysical Research*, 117, A05231. <https://doi.org/10.1029/2011ja017377>
- Kivelson, M. G., Bagenal, F., Kurth, W. S., Neubauer, F. M., Paranicas, C., & Saur, J. (2004). Magnetospheric interactions with satellites. In F. Bagenal, T. Dowling, & W. McKinnon (Eds.), *Jupiter: The planet, satellites, and magnetosphere* (pp. 513–536). Cambridge University Press.
- Liuzzo, L., Poppe, A. R., Halekas, J. S., Simon, S., & Cao, X. (2021). Investigating the Moon's interactions with the terrestrial magnetotail lobe plasma. *Geophysical Research Letters*, 48, e2021GL093566. <https://doi.org/10.1029/2021GL093566>
- Malaspina, D. M., Horányi, M., Zaslavsky, A., Goetz, K., Wilson, L. B., III, & Kersten, K. (2014). Interplanetary and interstellar dust observed by the Wind/WAVES electric field instrument. *Geophysical Research Letters*, 41, 266–272. <https://doi.org/10.1002/2013gl058786>

- Manka, R. H. (1973). Plasma and potential at the lunar surface. In R. J. L. Grard (Ed.), *Photon and particle interactions with surfaces in space* (Vol. 37, pp. 347–361). Astrophysics and Space Science Library. https://doi.org/10.1007/978-94-010-2647-5_22
- McBride, N., & McDonnell, J. A. M. (1999). Meteoroid impacts on spacecraft: Sporadics, streams, and the 1999 Leonids. *Planetary and Space Science*, 47, 1005–1013. [https://doi.org/10.1016/S0032-0633\(99\)00023-9](https://doi.org/10.1016/S0032-0633(99)00023-9)
- McFadden, J. P., Carlson, C. W., Larson, D., Bonnelli, J., Mozer, F., Angelopoulos, V., et al. (2008). THEMIS ESA first science results and performance issues. *Space Science Reviews*, 141, 477–508. <https://doi.org/10.1007/s11214-008-9433-1>
- McFadden, J. P., Carlson, C. W., Larson, D., Ludlam, M., Abiad, R., Elliott, B., et al. (2008). The THEMIS ESA plasma instrument and in-flight calibration. *Space Science Reviews*, 141, 277–302. <https://doi.org/10.1007/s11214-008-9440-2>
- Mozer, F. S., Agapitov, O. V., Bale, S. D., Bonnelli, J. W., Goetz, K., Goodrich, K. A., et al. (2020). Time domain structures and dust in the solar vicinity: Parker solar probe observations. *The Astrophysical Journal Supplement Series*, 246(2), 50. <https://doi.org/10.3847/1538-4365/ab5e4b>
- Nénon, Q., Poppe, A. R., Rahmati, A., Lee, C. O., McFadden, J. P., & Fowler, C. M. (2019). Phobos surface sputtering as inferred from MAVEN ion observations. *Journal of Geophysical Research: Planets*, 124, 3385–3401. <https://doi.org/10.1029/2019JE006197>
- Nishino, M. N., Harada, Y., Saito, Y., Tsunakawa, H., Takahashi, F., Yokota, S., et al. (2017). Kaguya observations of the lunar wake in the terrestrial foreshock: Surface potential change by bow-shock reflected ions. *Icarus*, 293, 45–51. <https://doi.org/10.1016/j.icarus.2017.04.005>
- Oberst, J., & Nakamura, Y. (1987). Distinct meteoroid families identified on the lunar seismograms. *Journal of Geophysical Research*, 92(B4), E769–E773. <https://doi.org/10.1029/JB092iB04p0E769>
- Piquette, M., & Horányi, M. (2017). The effect of asymmetric surface topography on dust dynamics on airless bodies. *Icarus*, 291, 65–74. <https://doi.org/10.1016/j.icarus.2017.03.019>
- Pokorný, P., Janches, D., Brown, P. G., & Hormaechea, J. L. (2017). An orbital meteoroid stream survey using the Southern Argentina Agile Meteor Radar (SAAMER) based on a wavelet approach. *Icarus*, 290, 162–182. <https://doi.org/10.1016/j.icarus.2017.02.025>
- Pokorný, P., Janches, D., Sarantos, M., Szalay, J. R., Horányi, M., Nesvorný, D., & Kuchner, M. J. (2019). Meteoroids at the Moon: Orbital properties, surface vaporization, and impact ejecta production. *Journal of Geophysical Research: Planets*, 124, 752–778. <https://doi.org/10.1029/2018JE005912>
- Pokorný, P., Sarantos, M., & Janches, D. (2018). A comprehensive model of the meteoroid environment around mercury. *The Astrophysical Journal*, 863(1), 31. <https://doi.org/10.3847/1538-4357/aad051>
- Poppe, A. R. (2016). An improved model for interplanetary dust fluxes in the outer Solar System. *Icarus*, 264, 369–386. <https://doi.org/10.1016/j.icarus.2015.10.001>
- Poppe, A. R., Halekas, J. S., Delory, G. T., Farrell, W. M., Angelopoulos, V., McFadden, J. P., et al. (2012). A comparison of ARTEMIS observations and particle-in-cell modeling of the lunar photoelectron sheath in the terrestrial magnetotail. *Geophysical Research Letters*, 39, L01102. <https://doi.org/10.1029/2011gl050321>
- Poppe, A. R., Halekas, J. S., & Horányi, M. (2011). Negative potentials above the day-side lunar surface in the terrestrial plasma sheet: Evidence of non-monotonic potentials. *Geophysical Research Letters*, 38, L02103. <https://doi.org/10.1029/2010gl046119>
- Poppe, A. R., & Horányi, M. (2010). Simulations of the photoelectron sheath and dust levitation on the lunar surface. *Journal of Geophysical Research*, 115, A08106. <https://doi.org/10.1029/2010ja015286>
- Raines, J. M., Gershman, D. J., Zurbuchen, T. H., Sarantos, M., Slavin, J. A., Gilbert, J. A., et al. (2013). Distribution and compositional variations of plasma ions in Mercury's space environment: The first three Mercury years of MESSENGER observations. *Journal of Geophysical Research: Space Physics*, 118, 1604–1619. <https://doi.org/10.1029/2012JA018073>
- Roussos, E., Krupp, N., Krüger, H., & Jones, G. H. (2010). Surface charging of Saturn's plasma-absorbing moons. *Journal of Geophysical Research*, 115, A08225. <https://doi.org/10.1029/2010ja015525>
- Sibeck, D. G., Angelopoulos, V., Brain, D. A., Delory, G. T., Eastwood, J. P., Farrell, W. M., et al. (2011). *The ARTEMIS mission* (pp. 27–59). Springer. https://doi.org/10.1007/978-1-4614-9554-3_3
- Spahn, F., Albers, N., Hörning, M., Kempf, S., Krivov, A. V., Makuch, M., et al. (2006). Cassini dust measurements at Enceladus and implications for the origin of the E ring. *Science*, 311, 1416–1032. <https://doi.org/10.1016/j.pss.2006.05.022>
- Srama, R., Ahrens, T. J., Altobelli, N., Auer, S., Bradley, J. G., Burton, M., et al. (2004). The Cassini cosmic dust analyzer. *Space Science Reviews*, 114, 465–518.
- Sternovsky, Z., Chamberlin, P., Horányi, M., Robertson, S., & Wang, X. (2008). Variability of the lunar photoelectron sheath and dust mobility due to solar activity. *Journal of Geophysical Research*, 113, A10104. <https://doi.org/10.1029/2008ja013487>
- Stubbs, T. J., Farrell, W. M., Halekas, J. S., Burchill, J. K., Collier, M. R., Zimmerman, M. I., et al. (2014). Dependence of lunar surface charging on solar wind plasma conditions and solar irradiation. *Planetary and Space Science*, 90, 10–27. <https://doi.org/10.1016/j.pss.2013.07.008>
- Szalay, J. R., & Horányi, M. (2015). Annual variation and synodic modulation of the sporadic meteoroid flux to the Moon. *Geophysical Research Letters*, 42, 10580–10584. <https://doi.org/10.1002/2015gl066908>
- Szalay, J. R., & Horányi, M. (2016). Detecting meteoroid streams with an in-situ dust detector above an airless body. *Icarus*, 275, 221–231. <https://doi.org/10.1016/j.icarus.2016.04.024>
- Szalay, J. R., Pokorný, P., Bale, S. D., Christian, E. R., Goetz, K., Goodrich, K., et al. (2020). The near-Sun dust environment: Initial observations from Parker solar probe. *The Astrophysical Journal Supplement Series*, 246(27). <https://doi.org/10.3847/1538-4365/ab50c1>
- Szalay, J. R., Pokorný, P., Jenniskens, P., & Horányi, M. (2018). Activity of the 2013 Geminid meteoroid stream at the Moon. *Monthly Notices of the Royal Astronomical Society*, 474, 4225–4231. <https://doi.org/10.1093/mnras/stx3007>
- Wang, C.-P., Lyons, L. R., & Angelopoulos, V. (2014). Properties of low-latitude mantle plasma in the Earth's magnetotail: ARTEMIS observations and global MHD predictions. *Journal of Geophysical Research: Space Physics*, 119, 7264–7280. <https://doi.org/10.1002/2014JA020060>
- Whipple, E. C. (1981). Potentials of surfaces in space. *Reports on Progress in Physics*, 44. <https://doi.org/10.1088/0034-4885/44/11/002>
- Xu, S., Poppe, A. R., Halekas, J. S., Mitchell, D. L., McFadden, J. P., & Harada, Y. (2019). Mapping the lunar wake potential structure with ARTEMIS data. *Journal of Geophysical Research: Space Physics*, 124, 3360–3377. <https://doi.org/10.1029/2019JA026536>
- Ye, S.-Y., Vavereka, J., Nouzak, L., Sternovsky, Z., Zaslavsky, A., Pavlu, J., et al. (2019). Understanding Cassini RPWS antenna signals triggered by dust impacts. *Geophysical Research Letters*, 46(10), 950. <https://doi.org/10.1029/2019GL084150>
- Zimmerman, M. I., Farrell, W. M., Stubbs, T. J., Halekas, J. S., & Jackson, T. L. (2011). Solar wind access to lunar polar craters: Feedback between surface charging and plasma expansion. *Geophysical Research Letters*, 38, L19202. <https://doi.org/10.1029/2011gl048880>